Supporting information (S1)

Traffic-related enhancement of new particle growth in an urban tunnel

Fuyang Zhang [a], Jinsheng Zhang [b, *], Jiayuan Liu [a], Yajun Wu [e], Zongyan Lv[f], Kexin Liu [a], Bin Sun [a], Qijun Zhang [a], Lin Wu [a], Miao Tang [c], Ning Yang [c, *], Wei Hu [d], Hongjun Mao [a], Jianfei Peng [a, *]

a Tianjin Key Laboratory of Urban Transport Emission Research & State Environmental Protection Key Laboratory of Urban Ambient Air Particulate Matter Pollution Prevention and Control, College of Environmental Science and Engineering, Nankai University, Tianjin 300071, China

b School of Environmental Science and Safety Engineering, Tianjin University of Technology, Tianjin 300384, China

c Tianjin Eco-Environmental Monitoring Center, Tianjin 300191, China.

d Institute of Surface-Earth System Science, Tianjin University, Tianjin 300072, China

e National Engineering Research Center of Urban Environmental Pollution Control, Beijing Municipal Research Institute of Eco-Environmental Protection, Beijing 100037, China

f School of Energy and Power Engineering, Shandong University, Jinan 250061, China

Corresponding authors:

Jianfei Peng (J.F. Peng): pengjianfei@nankai.edu.cn

Jinsheng Zhang (J.S. Zhang): jinshengz@nankai.edu.cn

Ning Yang (N. Yang): 13820388835@163.com

Number of pages: 20

Number of equations: 13

Number of figures: 15

Number of tables: 6

S1. Particle number size distributions during the selected NPF event days

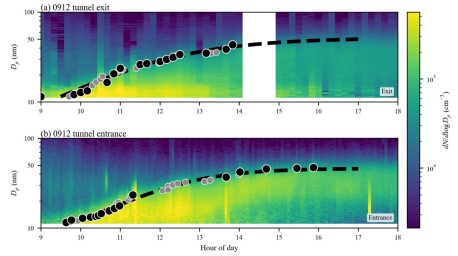

(i)

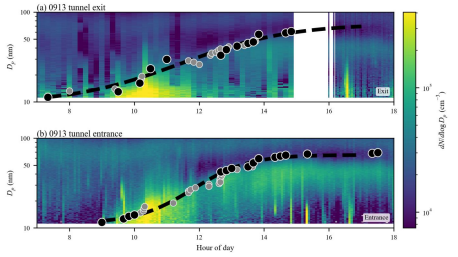

(ii)

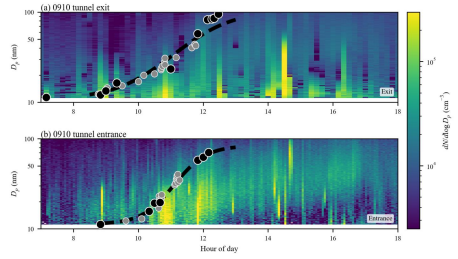

(iii)

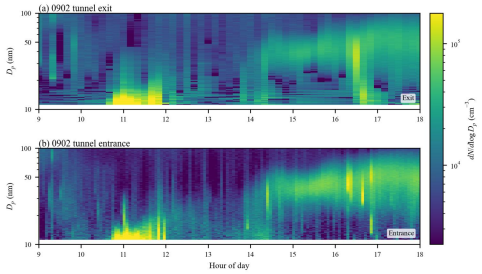

(iv)

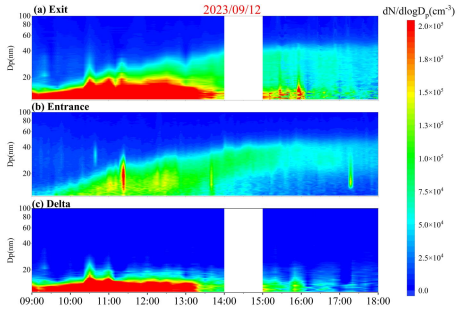

(v)

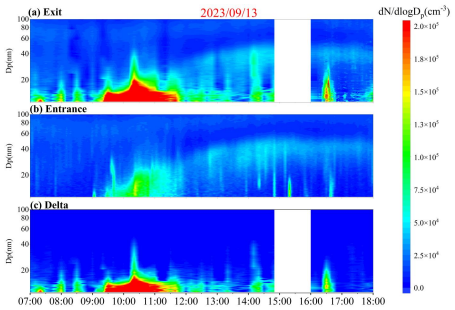

(vi)

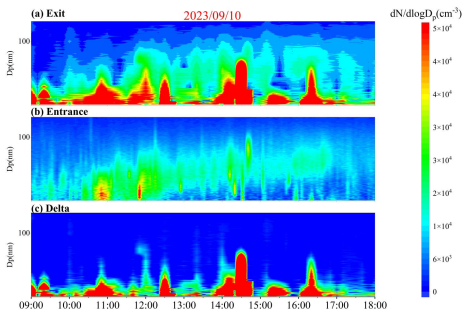

(vii)

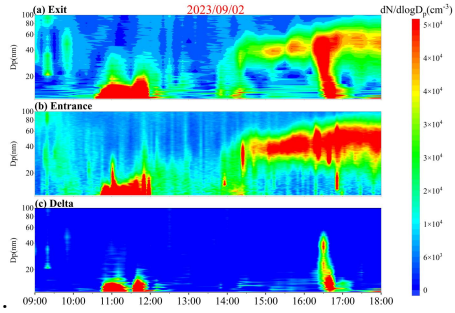

(viii)

Figure S1 **Event-specific diagnostic plots and corresponding event-resolved particle number size distributions during the tunnel campaign.** Panels (i)–(iv) correspond to the GR diagnostic plots for 2023/09/12, 2023/09/13, 2023/09/10, and 2023/09/02, respectively. For the three events used in the quantitative GR analysis, panels (a) and (b) show the measured PNSDs at the tunnel exit and entrance. Black circles indicate the primary 50% appearance-time points derived from 10 min averaged PNSDs, while gray circles indicate auxiliary 50% appearance-time points extracted from the original 3 min PNSDs. The dashed fitted trends were used to assess the continuity of the apparent particle-size evolution across the measured size range. Panels (v)–(viii) show the corresponding event-resolved daily

PNSDs for the same four dates using linear color scales, providing a complementary view of the absolute concentration patterns. Within each of panels (v)–(viii), subpanels (a)–(c) show the temporal evolution at the tunnel exit, tunnel entrance, and their difference (ΔPNC), respectively. Three events (2023/09/10, 2023/09/12, and 2023/09/13) showed sufficiently continuous particle growth within the measured 10–25 nm range and were included in the quantitative GR analysis, whereas 2023/09/02 was retained only for qualitative comparison.

S2. Observed sink-related quantities during the tunnel campaign

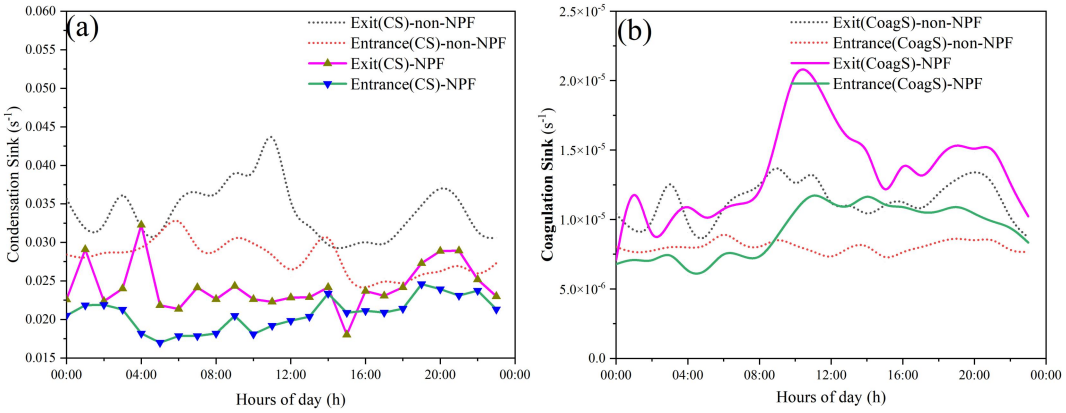

Figure S2 Diurnal variations of (a) condensation sink (CS) and (b) the 11.24 nm target-particle coagulation sink under selected event and non-event conditions during the tunnel campaign.

S3. Determination of GR-related quantities

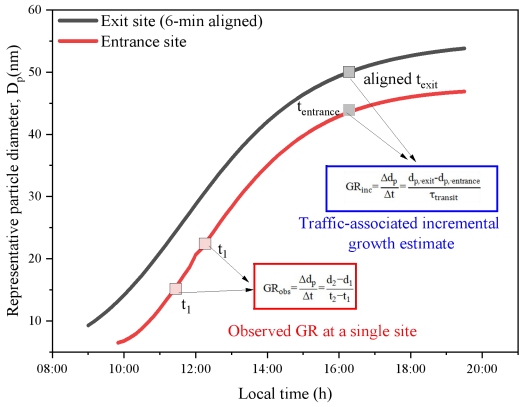

Figure S3 Schematic illustration of how the representative particle diameters and corresponding 50% appearance times were identified for the GR-related analysis. The figure shows the determination of the diameters used for the observed growth at the tunnel entrance and exit, as well as for the aligned entrance-exit comparison used to estimate the traffic-related incremental growth signal.

Table S1 Event-specific onset times and growth-rate estimates for the selected NPF event days during the tunnel campaign. GR_{obs} represents the site-specific observed apparent growth rate at the entrance and exit, derived independently using the 50% concentration appearance-time method. GR_{inc} represents the traffic-related incremental growth estimate derived from the 6-min time-aligned entrance-exit comparison. Only the three events with sufficiently continuous growth patterns were included in the quantitative analysis, whereas one additional event was retained only for qualitative comparison.

Date	Event type	Onset time at entrance	Onset time at exit	GR_{obs} at entrance (nm h^{-1})	GR_{obs} at exit (nm h^{-1})	GR_{inc}(nm h^{-1})	Included in quantitative analysis
2023/09/10	Continuous Growth	08:50	07:10	4.81	7.21	7.77	Yes
2023/09/12	Continuous Growth	09:38	09:00	6.09	6.91	7.32	Yes
2023/09/13	Continuous Growth	09:00	07:20	4.95	5.10	5.95	Yes
2023/09/02	Additional event	-	-	-	-	-	No

S4. Sink-related comparison during the 09:00–15:00 event window

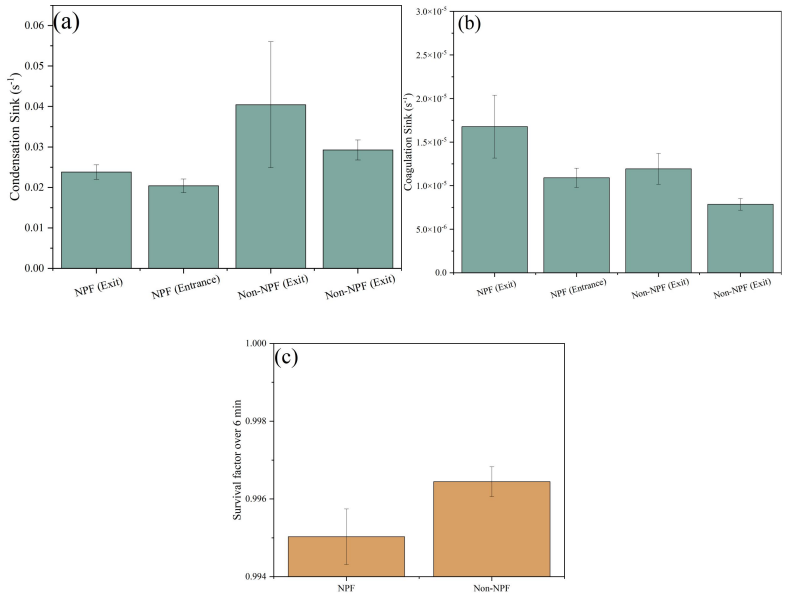

Figure S 4 Comparison of sink-related quantities between selected NPF and non-NPF conditions during the 09:00-15:00 event window. Panel (a) shows the mean condensation sink (CS) at the tunnel exit and entrance. Panel (b) shows the mean coagulation sink calculated for the smallest measured SMPS bin (11.24 nm), used here as an approximation for particles near the lower detection limit. Panel (c) shows the corresponding survival factors over the mean 6-min tunnel transit, estimated as $S=exp(-CoagS_{mean}\times\tau)$, where $CoagS_{mean}$ is the average of the entrance and exit values and τ is 360s.

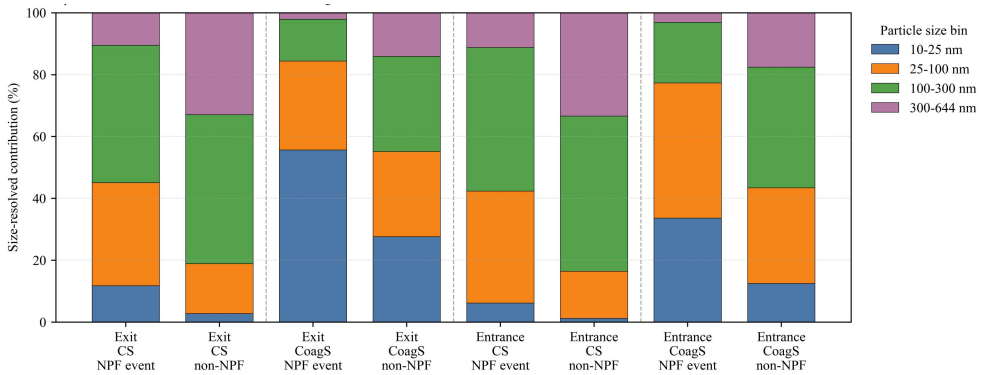

Figure S5 Size-resolved contributions to CS and the 11.24 nm target-particle CoagS during the 09:00–15:00 event window. CS was mainly influenced by larger-particle surface area, whereas the 11.24 nm

CoagS was strongly affected by nucleation/Aitken-mode number concentrations during NPF event periods.

S5. Measurement sites, setup, traffic fleet, and traffic-related pollutants

The tunnel measurements were carried out in Wujinglu Tunnel (WJL Tunnel, 117°12’15’’ E, 39°8’31’’) from September 1, 2023, to September 14, 2023. The station is situated at the heart of Tianjin's urban road network, offering insights into the traffic dynamics of a major northern Chinese megacity. (Figure S 6) The average daily traffic volume was about 13,000 vehicles, and the vehicle speed ranged from 30 to 40 km h^{-1}. The tunnel environment is in a semi-enclosed condition. The tunnel represents a traffic-dominated and semi-enclosed environment, which is suitable for examining particle enhancement and growth under strong vehicular influence. Two measurement sites were established near the entrance and exit of the WJL tunnel to compare particle evolution during tunnel transport.

During measurements, two scanning mobility particle sizers (SMPS 3082 TSI, USA) with long DMA (mode 3081A00) and two aerodynamic particle sizers (APS 3321 TSI, USA) were used to measure the PSD in the ranges of 10 nm to 10 μm. All instruments were carefully calibrated for consistency prior to the experiments. The details were illustrated in supporting information S6.

The vehicle-related pollutants (including NO_X, CO (carbon monoxide), and BC (black carbon)), were separately monitored using Thermo Scientific™ iQ (models 42i and 48i) and Aethalometer (model AE-33, Magee Scientific, USA). The mass concentrations of vehicle-related pollutants were shown in Figure S 9.

The portable meteorological station (VAISALA WXT 520, Helsinki, Finland) was used to measure relative humidity, atmospheric pressure, wind speed, and temperature both inside and outside of tunnel. The average wind speed within the tunnel is 1.5 m/s, and the distance between the two measurement points is 560 meters. To enable a comparison of particle growth features for approximately the same air mass at the tunnel entrance and exit, we subtracted 6 minutes from the time series data at the exit.

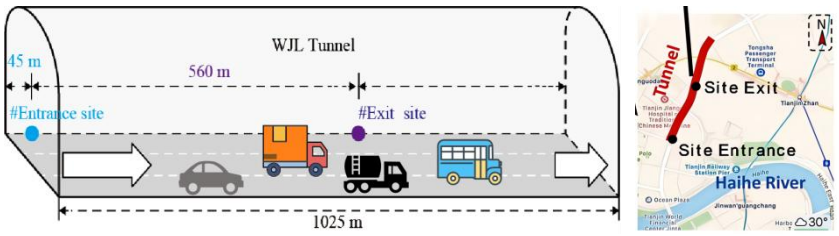

Figure S6 Measurement sites in the WJL Tunnel. (adapted from our previous study (Zhang et al., 2025; Zhang et al., 2024)).



Figure S 7 Measurement setup in the WJL Tunnel.

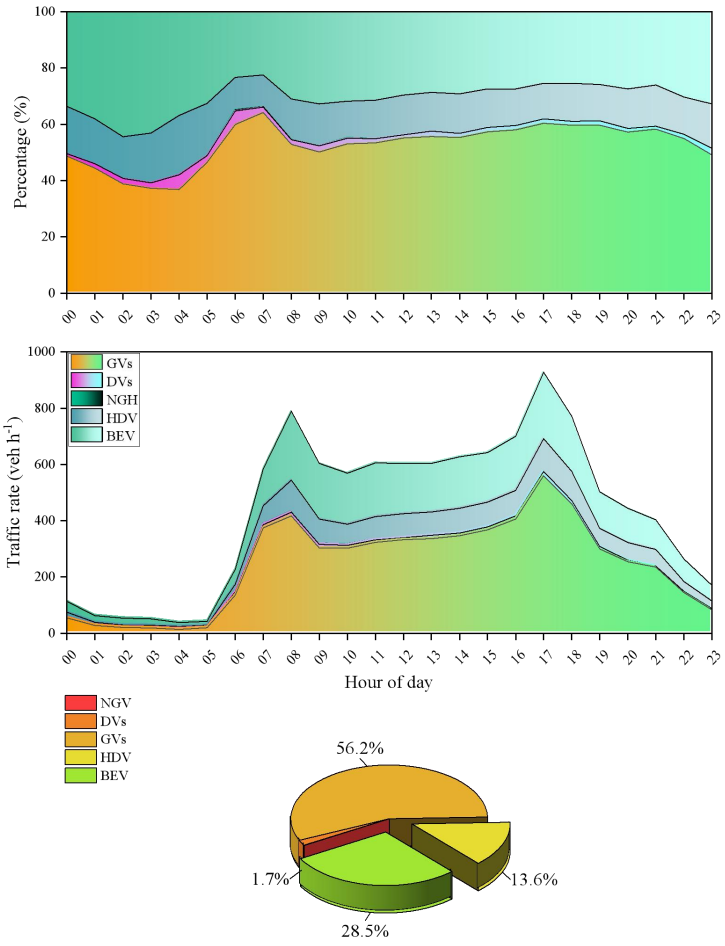

Figure S8 Traffic fleet across the Wujinglu tunnel in Tianjin. (adapted from our previous study

(Zhang et al., 2025; Zhang et al., 2024)). Vehicle types are abbreviated as NGV (denoting Natural Gas Vehicle), DV (Diesel Vehicle), GV (Gasoline Vehicle), HDV (Heavy-Duty Vehicle), and BEV (Battery Electric Vehicle).

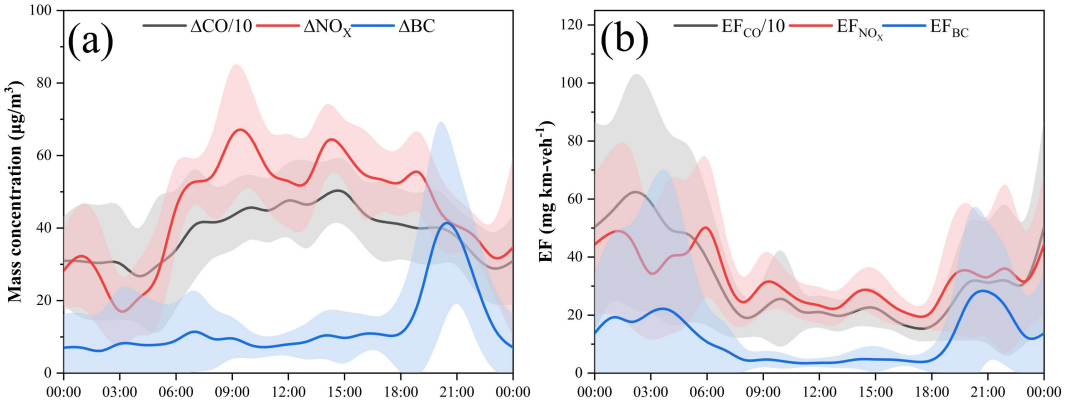

Figure S9 The diurnal mass concentration (a) and EF (b) of the vehicle-related pollutants (ΔCO, ΔNO_X and ΔBC included). (adapted from our previous study (Zhang et al., 2025; Zhang et al., 2024))

S6. Calibration of numerical spectrometers

To ensure data comparability, all scanning mobility particle sizers (SMPS 3082, TSI, USA) and aerodynamic particle sizers (APS, 3321 TSI, USA) were systematically calibrated prior to the campaign. During pre-dawn hours (04:00–05:00), when traffic flow was minimal and vehicle emissions negligible, the particle number concentration (PNC) differences between the tunnel entrance and exit were used to calibrate tunneling losses for particles larger than 40 nm.

Calibrating PNC for nucleation mode particles remained challenging due to their rapid atmospheric evolution through condensation and coagulation. To address this, two SMPS instruments were collocated at the tunnel entrance, sampling through a common inlet to monitor particle size distributions (PSD). A correction relationship for ultra-fine particles (<40nm) was derived from the concentration discrepancy between the compared SMPS. It should be noted that this approach may lead to a conservative estimate of traffic-related $PNC_{10\text{-}25}$ enhancement. Sensitivity analysis showed that a 1% increase in the correction coefficient led to approximately a 4.2% increase in total PNC, resulting in an increase of about 50 cm^{-3}. The details are illustrated in Table S2.

Table S2 **Correction coefficients for particle number concentration across the entire particle size range.** The correction coefficients for particles larger than 40 nm are highlighted in light red, while those for particles smaller than 40 nm are highlighted in light blue.

Diameter	Correction coefficient ($\frac{PNC\ exit}{PNC_{entrance}}$)	R^2
≤15.82 nm	2.218279373	0.862787989
15.82~18.94 nm	1.938969392	0.951794254
18.94~22.67 nm	1.4894241	0.797510828
22.67~27.14 nm	1.423094825	0.894043468
27.14~32.49 nm	1.366891636	0.917351842
32.49~38.89 nm	1.334794124	0.953185892
38.98~46.56 nm	1.385287585	0.836848248
46.56~55.73 nm	1.361868564	0.888875002
55.73~66.71 nm	1.379554554	0.883421593
66.71~79.89 nm	1.374458736	0.844992703
79.86~95.60 nm	1.339118157	0.719893527
95.60~114.44 nm	1.467057856	0.857773397
114.44~137.00 nm	1.443504667	0.789167534
137.00~164.00 nm	1.408957849	0.770437695
164.00~196.32 nm	1.386612863	0.806807704
196.32~235.01 nm	1.374646578	0.864637142
235.01~281.33 nm	1.267558603	0.773560981
281.33nm~336.78 nm	1.302666369	0.923888373
336.78~403.15 nm	1.254444194	0.945605124
403.15~482.61 nm	1.226124811	0.952266696
482.61~577.72 nm	1.236808477	0.883198788
577.72~643.00 nm	1.482261371	0.79998994

S7. Details of data processing

S7.1 GR- and formation-related quantities

To describe new-particle growth in the measured size range more clearly, two GR-related quantities were used in this study. First, the site-specific observed apparent growth rate at the tunnel entrance and exit was determined independently using the 50% concentration appearance-time method (Lehtipalo et al., 2014; Kulmala et al., 2012) :

$$GR_{obs}=\frac{\Delta d_p}{\Delta t}=\frac{d_2-d_1}{t_2-t_1} \quad (1)$$

where d_1 and d_2 are the representative particle diameters (nm) at times t_1 and t_2, respectively.

Second, to estimate the additional in-tunnel growth associated with traffic emissions, we used a time-aligned entrance-exit comparison based on the measured mean transit time of approximately 6 min. Specifically, the exit time series was shifted backward by 6 min so that the entrance and exit observations approximately represented the same air mass. Under this framework, a traffic-associated incremental growth estimate was derived as:

$$GR_{inc}=\frac{\Delta d_p}{\Delta t}=\frac{d_{p,\ exit,\ aligned}-d_{p,\ entrance}}{\tau_{transit}} \quad (2)$$

Where $d_{p,\ exit,\ aligned}$ and $d_{p,\ entrance}$ are the representative particle diameters (nm) of the aligned exit and entrance signals at the same event stage, and $\tau_{transit}$ is the mean air-mass transit time in the tunnel (approximately 6 min). Here, GR_{inc} is distinguished from the site-specific observed GR and is interpreted as a framework-based estimate of additional growth associated with in-tunnel traffic emissions.

The particle formation rate reflects the appearance of particles into a given detectable size range. In this study, the formation rate of 10 nm particles was calculated as:

$$J_{10}=\frac{dN_{10-25}}{dt}+CoagS_{17}*\ N_{10-25}+\frac{GR}{25-10}N_{10-25} \quad (3)$$

where N_{10-25} is the particle number concentration in the 10-25 nm size range, and $CoagS_{17}$ is the coagulation sink evaluated for a representative 17 nm target particle within this size range. In this study, $CoagS_{11.24}$ was used specifically for the near-10 nm sink comparison and survival-factor analysis in Figures S2, S4, and S5, whereas $CoagS_{17}$ was retained as the representative coagulation sink for the 10–25 nm interval in the J_{10} and J_{inc} calculations.

For the corresponding formation signal, the 10 nm particle formation rate associated with the traffic-driven enhancement was estimated as:

$$J_{10,\ inc}=\frac{N_{exit}-N_{entrance}}{\Delta t}+\frac{CoagS_{exit}+CoagS_{entrnace}}{2}*\ N_{entrance}+\frac{GR_{inc}}{25-10}N_{entrance} \quad (4)$$

where N_{exit} and $N_{entrance}$ are the particle number concentrations in the 10–25 nm size range at the exit and entrance sites, respectively; $CoagS_{exit}$ and $CoagS_{entrnace}$ are the corresponding coagulation sinks for particles in the same size range; and GR_{inc} is the traffic-associated incremental growth estimate defined in Eq. (2). This quantity should be interpreted as a framework-based estimate rather than a directly observed site-specific formation rate.

The analytical formula was used to estimate $J_{1.5}$ (Kerminen and Kulmala, 2002; Korhonen et al., 2011).

$$J_{1.5}=J_{10}*\ exp(\gamma\frac{CS}{GR}(\frac{1}{1.5nm}-\frac{1}{10nm})) \quad (5)$$

where CS represents the condensation sink (in units of m^{-2}) and γ is a coefficient having a value of 0.23 m^2 nm^2 h^{-1}. It should be noted that this theoretical estimate (Equation S5) may somewhat underestimate nucleation due to simplified treatment of molecular interactions within freshly formed clusters

S7.2 Sink-related quantities and apparent production estimate

The condensation sink (CS) represents the condensing vapor sink caused by the existing particle population, which can be calculated by:

$$CS=2\pi D\sum_{d_p}\beta_{m.d_p}d_p N_{d_p} \quad (6)$$

where D is the diffusion coefficient of the sulfuric acid, $\beta_{m.d_p}$ is the transition-regime correction factor, dp is the geometric mean diameter for the size bin, and N_{d_p} is the particle concentration in the size bin.

CoagS (coagulation sink) directly reflects the removal efficiency and rate of background atmospheric particles on newly formed particles. For particles of any given size, the CoagS can be expressed by the following equation:

$$CoagS_i=\sum_j K_{ij}N_j \quad (7)$$

Where K_{ij} is the Brownian coagulation coefficient between particles in the target size bin i and background particles in size bin j; N_j is the particle number concentration in size bin j.

To further evaluate whether coagulation-sink differences alone could explain the entrance–exit enhancement near the lower detection limit, we estimated a simplified apparent particle production term during tunnel transit. This term represents the additional particle production required to explain the observed increase in near-threshold particle number concentration after accounting for coagulation loss:

$$P_{app}\approx\frac{N_{exit}-N_{entrance}}{\tau}+k_{mean}N_{entrance} \quad (8)$$

$$\Delta P_{app}=P_{app,\ NPF}-P_{app,\ Non-NPF} \quad (9)$$

$$k_{mean}=\frac{CoagS_{exit}+CoagS_{entrance}}{2} \quad (10)$$

where P_{app} is a simplified apparent particle production estimate (cm^{-3} s^{-1}) required to explain the increase in near-threshold particle number concentration during tunnel transit after accounting for coagulation loss; N_{exit} and $N_{entrance}$ are the particle number concentrations (cm^{-3}) in the 11.24-25nm size range at the tunnel exit and entrance, respectively; τ is the mean air-mass transit time in the tunnel (360 s); ΔP_{app} is the difference in the apparent production estimate between NPF event and non-NPF conditions; $P_{app,\,NPF}$ and $P_{app,\,Non-NPF}$ are the corresponding apparent production estimates under selected event and non-event conditions, respectively; k_{mean} is the path-mean coagulation sink (s^{-1}), approximated by the average of the exit and entrance CoagS values; and $CoagS_{exit}$ and $CoagS_{entrance}$ are the coagulation sinks (s^{-1}) at the tunnel exit and entrance, respectively. This quantity is used here as a simplified apparent production estimate rather than a fully resolved physical source rate.

The scanning mobility particle sizer (SMPS) measured Stokes diameters in the range of 10-643 nm, while the aerodynamic particle sizer (APS) measured aerodynamic diameters in the range of 0.5-10 μm. To obtain a continuous particle number size distribution across the full measurement range, APS aerodynamic diameters (D_a) were converted to Stokes diameters (D_s) using the formula:

$$D_s = D_a \sqrt{\frac{\rho_0}{\rho_p}} \tag{11}$$

where ρ_0 is the reference density (1 g/cm³) and ρ_p is the particle density (1.4 g/cm³).

S8. Fitted Modes of Particle Number Size Distributions

Table S3 Mode fit parameters for mean size distribution during each measurement at each site. σ is the geometric standard deviation of the mode, N_m is the mode number concentration, and $D_{p,m}$ is the geometric mean diameter of the fitted log-normal mode.

Type	Fitted Mode 1			Fitted Mode 2			Fitted Mode 3		
	$D_{p,m}$ (nm)	N_m (cm^{-3})	σ	$D_{p,m}$ (nm)	N_m (cm^{-3})	σ	$D_{p,m}$ (nm)	N_m (cm^{-3})	σ
PNC in Exit (NPF event)	7.9	$1.42*10^5$	1.59	32.6	$1.49*10^4$	1.75	121.8	$2.27*10^3$	1.75
PNC in Entrance (NPF event)	10.9	$2.78*10^4$	1.97	37.4	$9.48*10^3$	1.85	130.1	$1.82*10^3$	1.45
ΔPNC (NPF event)	6.9	$1.53*10^5$	1.59	61.1	$7.56*10^2$	1.75	151.5	7	1.4
ΔPNC (non-NPF event)	7.8	$6.51*10^4$	1.56	35.5	$1.49*10^3$	1.98	×	×	×

Traffic-related enhancement	11.2	1.67*10^4	1.24	×	×	×	×	×	×

S9. Particle number concentrations on non-NPF days

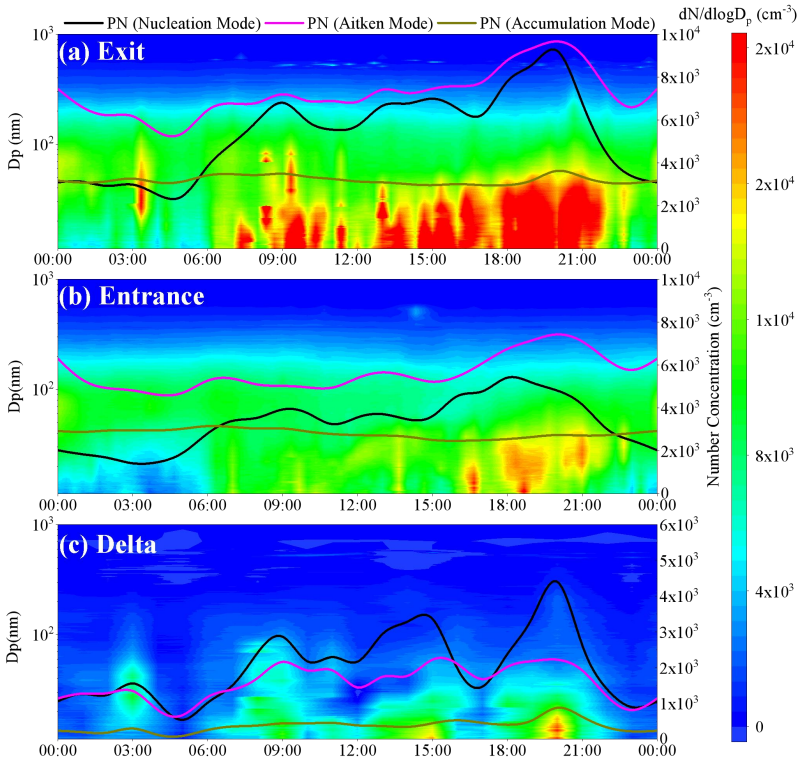

Figure S10 Diurnal variation of ultra-fine and fine PNC on the non-NPF days. The size spectra (ranging from 10 nm to 643 nm) in tunnel exit (a), entrance (b), and difference between entrance and exit (c). Note: NMP denotes particles in the measured 10-25 nm fraction in this figure.

S10. Source apportionment of particle number concentrations under the subtraction framework

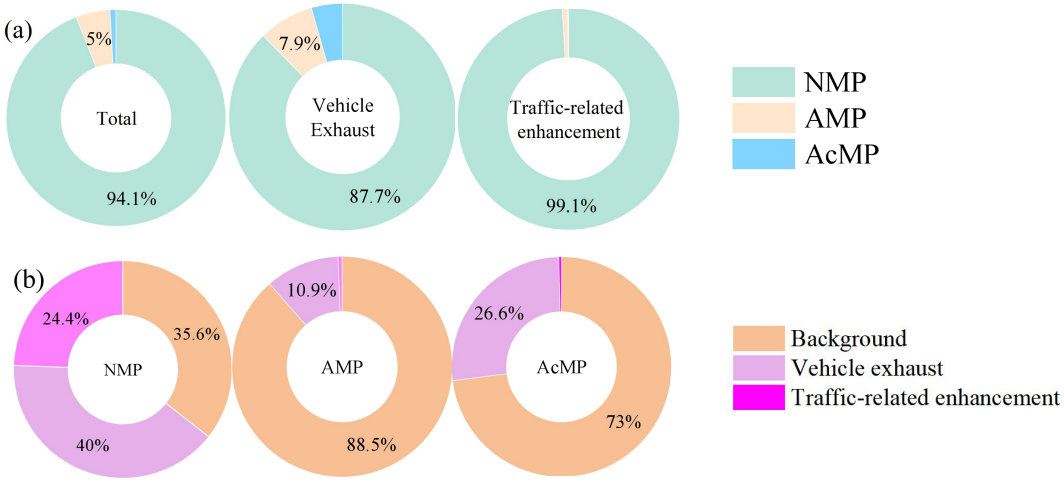

Figure S11 Source apportionment of the PNC emissions in WJL tunnel. Panel (a) illustrates the

composition of NPF-event reference, traffic-related enhancement, and vehicle-exhaust reference, while panel (b) shows the composition of nucleation mode particles (NMPs, 10-25nm), Aitken mode particles (AMPs), and accumulation mode particles (AcMPs).

S11. Comparison of traffic-related formation rates with previous in-situ studies

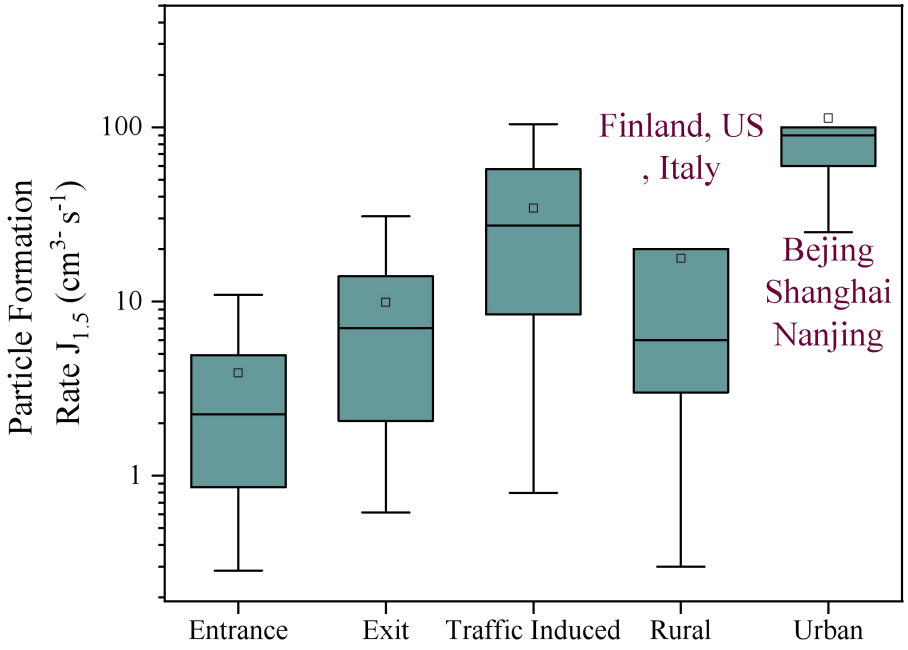

Figure S12 Comparison of traffic-related formation rates in the tunnel and previous in-situ studies (Deng et al., 2020; Yu et al., 2016; Yao et al., 2018; Kontkanen et al., 2016; Boulon et al., 2010; Yu et al., 2014).

S12. Dynamic VBS growth-model calculation

S12.1 Dynamic VBS model setup and inputs

To evaluate whether traffic-related lower-volatility condensable vapors could physically sustain the observed near-source particle growth, we applied the dynamic VBS growth model implemented in *aerosolpy.growth.VbsModel* (Stolzenburg et al., 2025; Stolzenburg et al., 2022). This calculation was used as the main physically constrained sensitivity test, whereas the mass-supply estimate was retained only as a supplementary check.

The model inputs were constructed from the tunnel entrance–exit organic concentration increments resolved by $\log_{10}C^*$ bins. The volatility-resolved organic data were constrained by related chassis-dynamometer measurements of gasoline and diesel vehicles, in which gas- and particle-phase organics were characterized by GC×GC-TOFMS and assigned into VBS bins (Wu et al., 2025). The $\log_{10}C^*<0$ bins were used as the lower-volatility traffic-related organic input in the

base simulation. Additional sensitivity cases included $\log_{10}C^*<0$, ±1 bin volatility shifts, particle-phase diffusion limitation, and seed-interaction assumptions.

Because the observational constraint corresponds to growth from approximately 11.2 to 11.9 nm during the mean 6-min tunnel transit, rather than growth from newly formed molecular clusters, the initial particle diameter in the model was set to 11.2 nm. The model-predicted diameter change over 0-6 min was then converted to an effective growth rate and compared with the observed traffic-related incremental growth estimate, GR_{inc} = 7.0 nm h^{-1}.

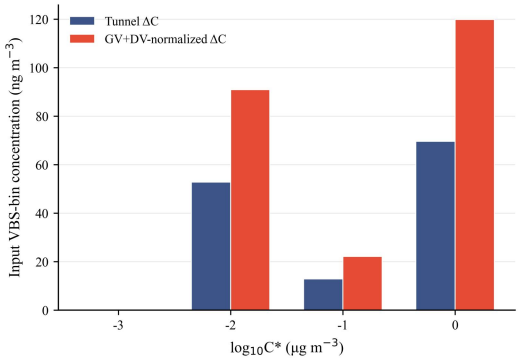

Figure S13 VBS-bin organic vapor inputs used in the aerosolpy dynamic VBS growth calculation. The blue bars show the tunnel entrance-exit organic concentration increments (Tunnel ΔC), and the red bars show the GV+DV-normalized ΔC sensitivity case. Concentrations are shown for each log10C* bin. The log10C*<0 bins were used as the lower-volatility traffic-related organic pool in the base VBS growth simulations, whereas the $\log_{10}C^*\leq0$ and GV+DV-normalized cases were used as sensitivity scenarios.

S12.2 Model-predicted growth rates

Using the direct tunnel ΔC for lower-volatility organics defined by $\log_{10}C^*<0$, the *aerosolpy base simulation* predicted an effective 0-6 min growth rate of 12.1 nm h^{-1}. When the volatility distribution was shifted by ±1 bin, the predicted growth rates ranged from 6.3 to 13.7 nm h^{-1}, approaching the observed GR_{inc} of 7.0 nm h^{-1}. Even under a strong particle-phase diffusion-limitation sensitivity case, the predicted growth rate remained approximately 8.4 nm h^{-1}, still comparable to the observed value. All VbsModel simulations include the Kelvin effect by default.

These results indicate that traffic-related lower-volatility condensable vapors were physically capable of supporting the observed near-source growth under the adopted dynamic VBS framework. This calculation is used as a physical plausibility test and does not identify the responsible molecules or exclude contributions from OOMs, amines, sulfuric acid, or other low-volatility vapors.

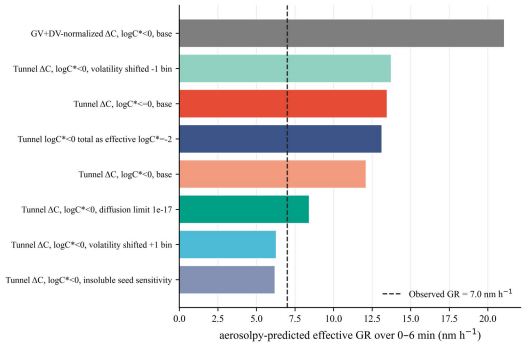

Figure S14 Aerosolpy-predicted effective growth rates under different VBS sensitivity scenarios. Effective growth rates were calculated from the model-predicted diameter change over the 0-6 min tunnel transit, with the initial particle diameter set to 11.2 nm. The vertical dashed line indicates the observed traffic-related incremental growth estimate, GR_{inc} = 7.0 nm h^{-1}, corresponding to growth from 11.2 to 11.9 nm over 6 min. The base simulation using the direct tunnel ΔC for the $log_{10}C^{*}<0$ lower-volatility organic pool predicted an effective growth rate of 12.1 nm h^{-1}, while the ±1 bin volatility sensitivity gave 6.3-13.7 nm h^{-1}. All VbsModel simulations include the Kelvin effect by default.

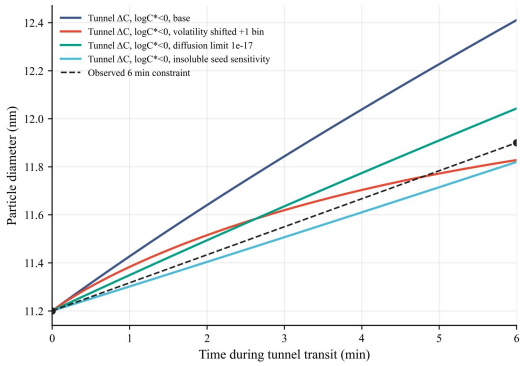

Figure S15 Aerosolpy-predicted particle growth trajectories during the 6-min tunnel transit. The trajectories show the dynamic VBS-model predictions for selected sensitivity scenarios using an initial particle diameter of 11.2 nm. The black dashed line and symbols indicate the observational 6-min constraint derived from GRinc = 7.0 nm h^{-1}, corresponding to growth from 11.2 to 11.9 nm. These trajectories are used only to evaluate whether the volatility-resolved traffic-related organic vapor increments can sustain the observed near-source growth during tunnel transit, and should not be interpreted as post-tunnel particle evolution.

S12.3 Supplementary mass-supply check

To evaluate whether vehicle-emitted lower-volatility condensable vapors were sufficient, in terms of mass supply, to support the observed near-source particle growth, we performed a simplified VBS-based mass-balance estimate. The potential concentration increment of lower-volatility organics in the tunnel was estimated as:

$$\Delta C = \frac{(\sum_v f_v EF^{km}_{v,Lvoc}) * L * N}{Q * T} * 10^6 \quad (12)$$

where ΔC is the LVOC concentration increment in the tunnel (ng m^{-3}), N is the daily traffic volume (vehicles day^{-1}); L is the entrance–exit distance (km); f_v is the fleet fraction of vehicle type v; $EF^{km}_{v,Lvoc}$ is the mileage-based emission factor of lower-volatility organics for vehicle type v (mg km^{-1}); Q is the effective ventilation rate (m^3 s^{-1}); T is 86400 s day^{-1}; and 10^6 converts mg m^{-3} to ng m^{-3}.

The condensed mass required to support the observed particle growth was estimated from particle-volume growth and mass conservation:

$$\Delta M_{grow} = N_{grow} \rho_p \frac{\pi}{6} (D_2^3 - D_1^3) * 10^{-6} \quad (13)$$

where ΔM_{grow} is the required condensed mass (ng m^{-3}), N_{grow} is the particle number concentration (cm^{-3}), ρ_p is particle density (g cm^{-3}), and D_1 and D_2 are particle diameters before and after growth (nm)

Here, D_1 was set to 11.2 nm, corresponding to the peak diameter of the traffic-related enhancement near the lower detection limit. Based on GR_{inc}=7.0nm h^{-1} and the approximately 6-min tunnel transit time, the diameter growth was approximately 0.7 nm. Using the observed entrance-exit PNC increment and exit PNC as observational constraints, the required condensed mass was estimated to be 4.9-10.1 ng m^{-3}, lower than the estimated potential lower-volatility organic supply of approximately 66 ng m^{-3}. This mass-supply estimate is consistent with the dynamic VBS model results, but it is used only as a supplementary plausibility check and not as the primary model-based evidence.

297 Table S4 Parameters used in the VBS-based mass-balance estimate

Parameter	Value	Description
GR_{inc}	7.0 nm h^{-1}	Traffic-related incremental growth estimate
τ	6 min	Mean tunnel transit time
D_1	11.2 nm	Representative initial diameter
D_2	11.9 nm	Diameter after 0.7 nm growth
ρ_p	1.4 g cm^{-3}	Particle density
N_{grow}	2.4-4.9 × 10^4 cm^{-3}	Observational PNC constraints
ΔM_{grow}	4.9-10.1 ng m^{-3}	Required condensed mass
ΔC	~66 ng m^{-3}	Estimated lower-volatility organic supply
$EF_{GV,LVOCS}$	0.126 mg km^{-1}	Mileage-based lower-volatility organic emission factor for gasoline vehicles, using $Log_{10}C^*<0$ as the operational lower-volatility pool (Wu et al., 2025; Liu et al., 2024)
$EF_{DV,LVOCS}$	0.099 mg km^{-1}	Mileage-based lower-volatility organic emission factor for diesel vehicles, using $Log_{10}C^*<0$ as the operational lower-volatility pool (Wu et al., 2025; Liu et al., 2024)

298

299 **S13. Meteorological and air-quality context of the tunnel observation**

300 Meteorological and air-quality conditions were summarized to characterize the entrance-exit
301 comparison during the selected event windows. Meteorological variables, including temperature,
302 relative humidity, and wind speed, were obtained from the nearby meteorological station (54511),

303 the tunnel entrance, and the tunnel exit. Air-quality indicators, including $PM_{2.5}$, NO_X, CO, and O_3,
304 were obtained from the nearby air-quality station, the tunnel entrance, and the tunnel exit. Values
305 are reported as mean ± SD during 09:00-15:00 for the selected NPF event days and non-NPF days
306 (Tables S5 and S6). These data show that the entrance site was not equivalent to open urban
307 background air, because traffic-related indicators were generally higher at the entrance than at the
308 nearby station and further increased at the exit. Therefore, the entrance was used as a less
309 accumulated near-entrance reference for the entrance-exit comparison under selected tunnel
310 conditions, rather than as a true background site.

311 Table S5 Meteorological context during selected NPF event periods (9:00~15:00).

Variable	Unit	Condition	Nearby station	Entrance	Exit
Temperature	°C	NPF event days	26.7 ± 2.7	27.1 ± 2.8	29.0 ± 0.7
Temperature	°C	Non-NPF days	29.2 ± 3.1	29.3 ± 2.9	28.7 ± 1.3
RH	%	NPF event days	66.1 ± 11.4	43.1 ± 18.3	46.9 ± 9.5
RH	%	Non-NPF days	61.0 ± 10.7	51.9 ± 11.3	48.5 ± 7.0
Wind speed	$m\ s^{-1}$	NPF event days	1.8 ± 0.1	2.1 ± 0.2	1.5 ± 0.4
Wind speed	$m\ s^{-1}$	Non-NPF days	1.6 ± 0.4	2.0 ± 0.2	1.1 ± 0.4

312 Table S6 Air-quality context during NPF event periods (9:00~15:00).

Variable	Unit	Condition	Nearby station	Entrance	Exit
$PM_{2.5}$	$\mu g\ m^{-3}$	NPF event days	20.8 ± 18.7	69.2 ± 26.7	105.5 ± 28.9
$PM_{2.5}$	$\mu g\ m^{-3}$	Non-NPF days	34.5 ± 15.7	103.7 ± 74.9	141.5 ± 34.8
NOx	ppb	NPF event days	9.9 ± 3.0	17.1 ± 5.4	52.2 ± 13.1
NOx	ppb	Non-NPF days	10.0 ± 5.2	15.0 ± 8.9	47.6 ± 13.4
CO	ppb	NPF event days	571.5 ± 108.3	691.5 ± 230.9	1083.0 ± 210.3
CO	ppb	Non-NPF days	591.4 ± 119.5	827.6 ± 189.0	1238.6 ± 177.5
O_3	ppb	NPF event days	70.6 ± 27.5	44.8 ± 17.1	2.2 ± 2.7
O_3	ppb	Non-NPF days	72.9 ± 19.5	71.0 ± 17.9	9.7 ± 4.0

313

References

Boulon, J., Sellegri, K., Venzac, H., Picard, D., Weingartner, E., Wehrle, G., Collaud Coen, M., Bütikofer, R., Flückiger, E., Baltensperger, U., and Laj, P.: New particle formation and ultrafine charged aerosol climatology at a high altitude site in the Alps (Jungfraujoch, 3580 m a.s.l., Switzerland), Atmospheric Chemistry and Physics, 10, 9333–9349, 10.5194/acp-10-9333-2010, 2010.

Deng, C., Fu, Y., Dada, L., Yan, C., Cai, R., Yang, D., Zhou, Y., Yin, R., Lu, Y., and Li, X.: Seasonal characteristics of new particle formation and growth in urban Beijing, Environmental Science & Technology, 54, 8547–8557, 2020.

Kerminen, V.-M. and Kulmala, M.: Analytical formulae connecting the "real" and the "apparent" nucleation rate and the nuclei number concentration for atmospheric nucleation events, Journal of Aerosol Science, 33, 609–622, 2002.

Kontkanen, J., Järvinen, E., Manninen, H. E., Lehtipalo, K., Kangasluoma, J., Decesari, S., Gobbi, G. P., Laaksonen, A., Petäjä, T., and Kulmala, M.: High concentrations of sub-3nm clusters and frequent new particle formation observed in the Po Valley, Italy, during the PEGASOS 2012 campaign, Atmospheric Chemistry and Physics, 16, 1919–1935, 10.5194/acp-16-1919-2016, 2016.

Korhonen, H., Sihto, S.-L., Kerminen, V.-M., and Lehtinen, K.: Evaluation of the accuracy of analysis tools for atmospheric new particle formation, Atmospheric Chemistry and Physics, 11, 3051–3066, 2011.

Kulmala, M., Petäjä, T., Nieminen, T., Sipilä, M., Manninen, H. E., Lehtipalo, K., Dal Maso, M., Aalto, P. P., Junninen, H., and Paasonen, P.: Measurement of the nucleation of atmospheric aerosol particles, Nature Protocols, 7, 1651–1667, 2012.

Lehtipalo, K., Leppä, J., Kontkanen, J., Kangasluoma, J., Franchin, A., Wimnner, D., Schobesberger, S., Junninen, H., Petäjä, T., and Sipilä, M.: Methods for determining particle size distribution and growth rates between 1 and 3 nm using the Particle Size Magnifier, Boreal Environment Research, 19, 215–236, 2014.

Liu, P., Wu, Y., Li, Z., Lv, Z., Zhang, J., Liu, Y., Song, A., Wang, T., Wu, L., and Mao, H.: Tailpipe volatile organic compounds (VOCs) emissions from Chinese gasoline vehicles under different vehicle standards, fuel types, and driving conditions, Atmospheric Environment, 323, 120348, 2024.

Stolzenburg, D., Wang, M., Schervish, M., and Donahue, N. M.: Tutorial: Dynamic organic growth modeling with a volatility basis set, Journal of Aerosol Science, 166, 106063, 2022.

Stolzenburg, D., Sarnela, N., Bianchi, F., Cai, J., Cai, R., Cheng, Y., Dada, L., Donahue, N. M., Grothe, H., and Holm, S.: Incomplete mass closure in atmospheric nanoparticle growth, npj Climate and Atmospheric Science, 8, 75, 2025.

Wu, Y., Liu, P., Wang, Y., Wang, X., Zhang, J., Liu, Y., Zhang, J., Wu, L., Wang, T., and Mao, H.: Intermediate and semi-volatility organic compounds (I/SVOCs) emission from Chinese vehicles: volatility distribution, influencing factors, and implication for SOA formation, Frontiers of Environmental Science & Engineering, 19, 70, 2025.

Yao, L., Garmash, O., Bianchi, F., Zheng, J., Yan, C., Kontkanen, J., Junninen, H., Mazon, S. B., Ehn, M., and Paasonen, P.: Atmospheric new particle formation from sulfuric acid and amines in a Chinese megacity, Science, 361, 278–281, 2018.

Yu, H., Zhou, L., Dai, L., Shen, W., Dai, W., Zheng, J., Ma, Y., and Chen, M.: Nucleation and growth of sub-3 nm particles in the polluted urban atmosphere of a megacity in China, Atmospheric Chemistry and Physics, 16, 2641–2657, 10.5194/acp-16-2641-2016, 2016.

Yu, H., Ortega, J., Smith, J. N., Guenther, A. B., Kanawade, V., You, Y., Liu, Y., Hosman, K., Karl, T., and Seco, R.: New particle formation and growth in an isoprene-dominated Ozark forest: From sub-5 nm

to CCN-active sizes, Aerosol Science and Technology, 48, 1285–1298, 2014.
Zhang, F., Peng, J., Zhang, J., Liu, J., Wu, Y., Liu, P., Liu, K., Sun, B., Zhang, Q., Wu, L., Yang, N., Hu, W., and Mao, H.: Real world particle size distribution from vehicle fleet and implication on emission control, npj Clean Air, 1, 8, 10.1038/s44407-025-00007-8, 2025.
Zhang, J., Peng, J., Song, A., Du, Z., Guo, J., Liu, Y., Yang, Y., Wu, L., Wang, T., Song, K., Guo, S., Collins, D., and Mao, H.: Secondary organic aerosol formation potential from vehicular non-tailpipe emissions under real-world driving conditions, Environmental Science & Technology, 58, 5419–5429, 10.1021/acs.est.3c06475, 2024.